# Spatial consistency of cell growth direction during organ morphogenesis requires CELLULOSE-SYNTHASE INTERACTIVE1

Corentin Mollier, Joanna Skrzydel, Dorota Borowska-Wykret, Mateusz Majda, Mateusz Dulski, Antoine Fruleux, Roman Wrzalik, Richard S Smith, Françoise Monéger, Dorota Kwiatkowska, et al.

# Spatial consistency of cell growth direction during organ morphogenesis requires CELLULOSE-SYNTHASE INTERACTIVE1

Corentin Mollier [1], Joanna Skrzydeł [2], Dorota Borowska-Wykret [2], Mateusz Majda [3], Mateusz Dulski [4, 5], Antoine Fruleux [1, 6], Roman Wrzalik [4, 5], Richard S. Smith [3], Françoise Monéger [1], Dorota Kwiatkowska [2 *], Arezki Boudaoud [1, 7 *]

1: Reproduction et développement des plantes, Université de Lyon, ENS de Lyon, UCB Lyon 1, CNRS, INRAE, 69364 Lyon Cedex, France

2: Institute of Biology, Biotechnology and Environmental Protection, University of Silesia in Katowice, Poland

3: John Innes Centre, Norwich Research Park, Colney Lane, Norwich, NR4 7UH, UK

4: Silesian Center for Education and Interdisciplinary Research, University of Silesia in Katowice, Poland

5: August Chełkowski Institute of Physics, University of Silesia in Katowice, Poland

6: LPTMS, CNRS, Université Paris-Saclay, 91405 Orsay Cedex, France

7: LadHyX, Ecole polytechnique, CNRS, IP Paris, 91128 Palaiseau Cedex, France

* Corresponding authors:

dorota.kwiatkowska@us.edu.pl, arezki.boudaoud@polytechnique.edu

## Abstract

Extracellular matrices generally contain fibril-like polymers that may be organized in parallel arrays. Although their role in morphogenesis has been recognized, it is still unclear how the subcellular control of fibril synthesis translates into well-defined organ shape. Here, we addressed this question using the *Arabidopsis* sepal as a model organ. In plants, cell growth is driven by turgor pressure and restrained by the extracellular matrix known as the cell wall. Cellulose is the main load-bearing component of the plant cell wall and cellulose microfibrils are thought to channel growth perpendicularly to their main orientation. We investigated the role of the guidance of cellulose synthesis by CELLULOSE SYNTHASE INTERACTIVE 1 (CSI1) in sepal morphogenesis. We observed that sepals are shorter in *csi1* mutants, although the newest cellulose microfibrils are more aligned in *csi1*. Surprisingly, cell growth anisotropy was similar in *csi1* and wild-type plants. We resolved this apparent paradox using polarized Raman microspectroscopy and live imaging of growing sepals. We found that CSI1 is required for spatial consistency of growth direction across the sepal and for the maintenance of overall organ elongation. We confirmed our conclusions at sepal scale, notably using bespoke mechanical assays. Our work illustrates how the subcellular regulation of the extracellular matrix may control morphogenesis at multiple scales.


Key words: cellulose, CSI1, morphogenesis, growth coordination, sepal

## Introduction

Living organisms display an amazing variety of forms. While a given form may be achieved through several morphogenetic trajectories, morphogenesis often involves elongation or anisotropic growth, i.e. more growth along one axis of the organ. Elongated forms may result from coordinated cell rearrangements such as intercalation[1,2], from patterned heterogeneity in the physical properties of cells[3–6], or from guidance of growth by a matrix surrounding cells or tissues, usually a material reinforced by fibrils[7–9]. Here, we consider the link between fibril arrangement and elongation.

The nature of fibrils and the guidance of fibril synthesis largely vary between kingdoms. In several rod-shaped bacteria, the synthesis of peptidoglycans is guided by MreB, an actin homologue, following membrane curvature[10,11] and driving bacterial elongation. In Drosophila oocytes, microtubules guide the polar secretion of collagen in the surrounding epithelium[8,9]. Collagen deposition is associated with a global rotation of the oocyte inside the matrix, which yields a circumferential arrangement of fibrils and a mechanically anisotropic extracellular matrix, which is required for oocyte elongation[7,12]. Finally in plants, cells are surrounded by a cell wall composed of cellulose microfibrils embedded in a matrix of pectins, hemicelluloses, and structural proteins. Cellulose microfibrils may lead to mechanical anisotropy of the cell wall and channel growth[13]. Despite increasing knowledge about the link between cellulose microfibrils arrangement and cellular growth[13–15], how this yields well-defined organ forms remains poorly understood.

Cellulose chains are polymerized at the plasma membrane by complexes of cellulose synthase (CESA) and bundle into microfibrils in the cell wall. CESA complexes are associated with other proteins such as KORRIGAN that is involved in targeting CESA to the membrane[16,17], CELLULOSE COMPANION 1 that stabilizes the microtubules guiding the CESA[18], and CELLULOSE SYNTHASE INTERACTIVE PROTEIN 1 (CSI1) that binds microtubules and CESA complexes[19–21]. Two genes closely related to *CSI1* have been identified: expression of *CSI2* is restricted to pollen, while mutations of *CSI3* yield no visible phenotype[22]. *csi1* mutant exhibits hyper aligned cellulose microfibrils in the hypocotyl[23], probably because in the absence of microtubule guidance, CESA are partly guided by previously deposited cellulose microfibrils[24]. Strangely, this hyper alignment of cellulose in *csi1* hypocotyls was not

associated with an increased cell/organ growth anisotropy[19,20] , questioning the link between microfibrils alignment and anisotropic growth. In this work we addressed this link, from cellular to tissue scale.

Growth of etiolated hypocotyls is highly stereotyped[5] and mostly uniaxial, limiting the use of the hypocotyl to explore the relation between cellulose microfibrils deposition and growth direction. We chose to investigate this relation in the Arabidopsis sepal, the green leaf-like organ that protects a flower before its opening. Sepal shape and size are robust[25], despite variability in areal cell growth[26,27] and putatively in growth direction. We studied the links between cellulose organization, growth anisotropy and main growth direction, from cell to organ scale, using *csi1* mutation to test our conclusions.

## Results

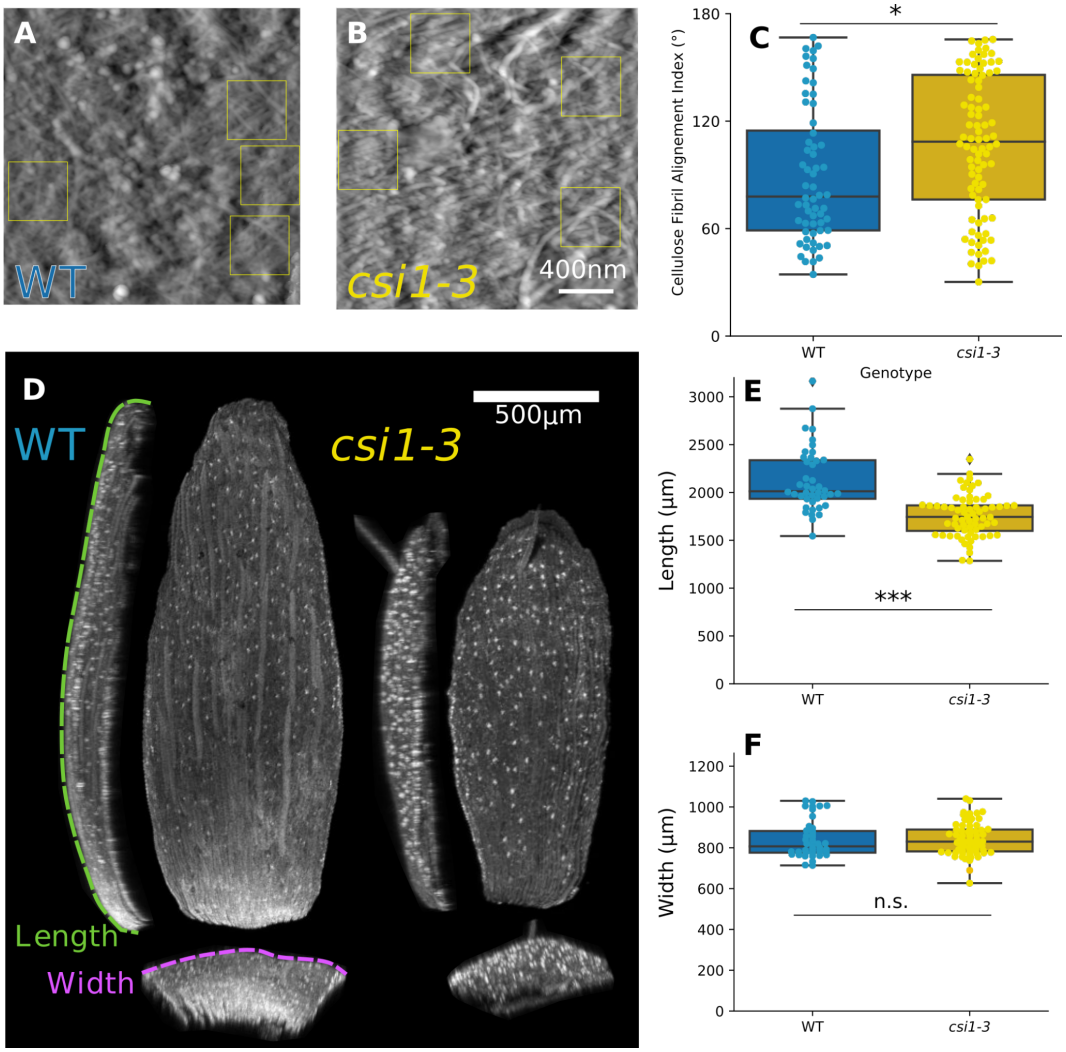


**Figure 1: Recently deposited cellulose microfibrils are more aligned in *csi1* than in wild-type (WT), but *csi1* sepals are shorter**

**A,B.** Representative topography maps, obtained with Atomic Force Microscopy (AFM), of WT and *csi1-3* outer epidermis cell wall imaged from the protoplast side after removing internal tissues and epidermis protoplasts of the sepal (maps corresponding to the median value of the alignment index for each genotype). Yellow squares outline regions used for the index assessment.

**C.** Alignment index of cellulose microfibrils, with high values corresponding to more aligned microfibrils. Boxplots for WT and *csi1-3* (N=5 and 6 stage 12 sepals and n=60 and 105 regions of 400nm×400nm from 9 and 14 cells, respectively; p-value of Mann-Whitney test = 0.005).

**D.** Representative front, top, and side views of WT and *csi1-3* fully grown sepals (stage 12 of flower development), obtained from projections of confocal images. Cell walls were stained using propidium iodide. The dotted lines show sepal maximal width and length as measured along the outer (abaxial) surface of the sepal.

**E,F.** Comparison of length and width of WT and *csi1-3* sepals, measured as in D (n=39 and 67, respectively. t-test p-values = $1\times10^{-10}$, 0.73, for length and width, respectively.)

Here and elsewhere, the boxes extend from the first to the third quartiles of the distributions, the line inside the box indicates the median, the whiskers span the full range of the data (except when outliers are present, corresponding to points further than 1.5 x interquartile range from the corresponding quartile), and the points correspond to individual values. Statistical significance: *= $p < 0.05$, **=$p < 0.005$, and ***= $p < 0.0005$.

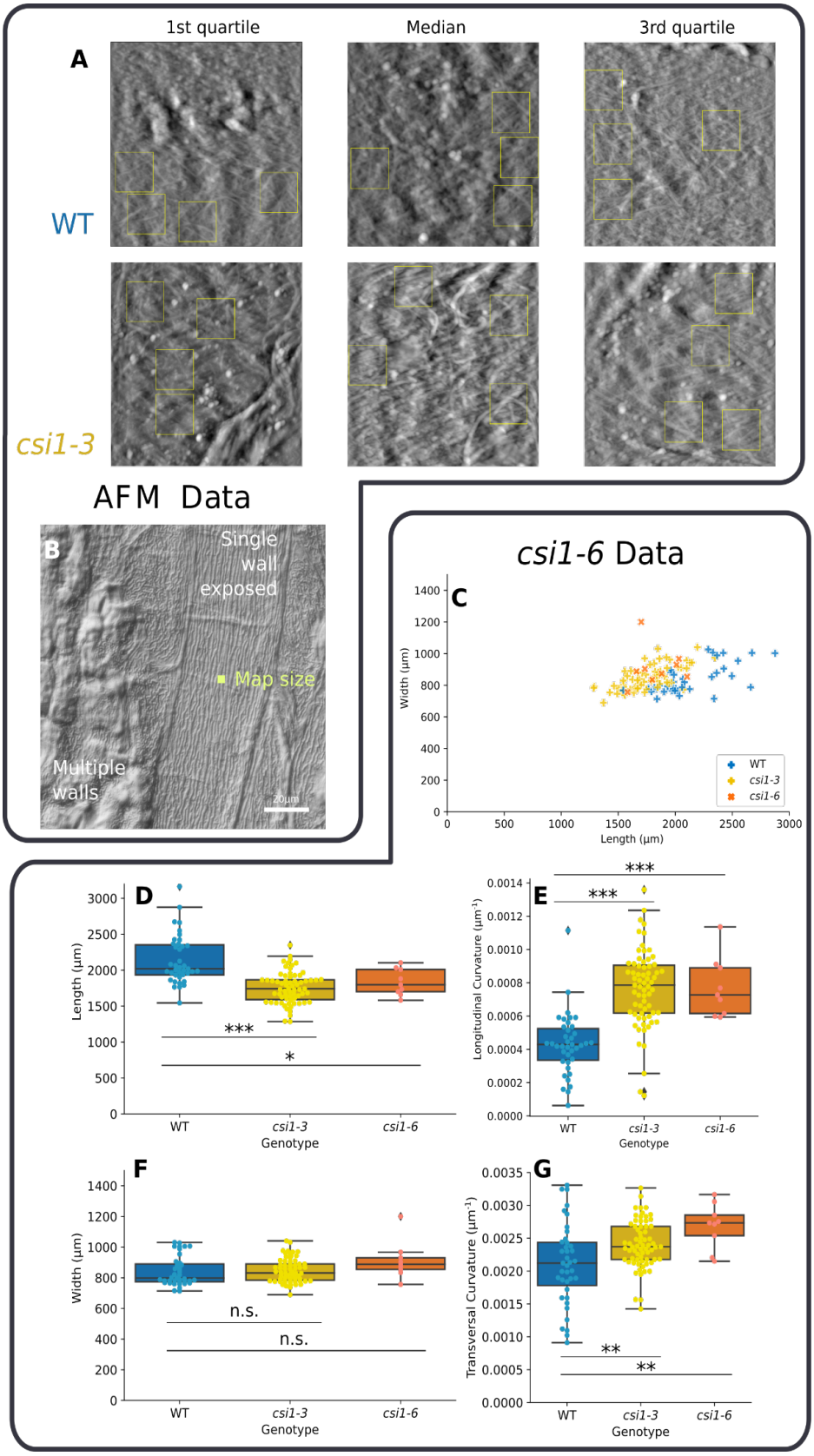


**Supplementary Figure 1:**

**A.** Atomic Force Microscopy (AFM) maps corresponding to first quartile, median, and third quartile for the alignment index (the first quartile corresponds to a low alignment index). Small yellow rectangles

show the areas with visible microfibrils used for the analysis. Whole map size = 2µm×2µm, single region analyzed = 400nm×400nm.

**B.** Differential interference contrast microscopy image of the samples analyzed in AFM. The yellow square near the image center indicates the size of an AFM map. The protoplast-facing surface of the outer periclinal wall is exposed in the cell slightly to the right, while the cells on the left are covered by walls of inner sepal cells (parenchyma). The lines that are visible in the background correspond to cuticular ridges that are present on the other side of the cell wall.

**C.** Length and width of individual WT, *csi1-3* and *csi1-6* sepals.

**D,E.** Comparison of length and width of WT, *csi1-3* and *csi1-6* sepals, measured as shown in Figure 1D (n=39, 67 and 9, respectively. t-test p-values between WT and *csi1-6* = 0.01, 0.06 for length and width. See legend of Figure 1 for the comparison with *csi1-3*.)

**F,G.** Comparison of curvatures along the main axes of the sepal. Curvature is defined as the inverse of the radius of a circle fitted to the center of the sepal (p-values of t-test for longitudinal curvature = $7\times10^{-12}$ and $8\times10^{-6}$ for comparison between WT and *csi1-3* or *csi1-6*, respectively. p values for transversal curvature = $2\times10^{-3}$ and $9\times10^{-3}$ for comparison between WT and *csi1-3* or *csi1-6*, respectively.)

## Cellulose microfibrils arrangement is more anisotropic in *csi1*

We first compared cellulose microfibrils patterns between the cell walls of WT and *csi1-3* sepals. To expose the inner surface of the outer epidermal wall before imaging, we gently scratched inner sepal tissues and removed protoplasts using chemical treatment, until we had only one cell-wall remaining. Because this method did not require grinding, this allowed us to keep track of the approximate position of the wall on the sepal, as well as to ensure the observation of the external wall of the epidermis, as confirmed by optical microscopy (**Fig S1B**). We then used Atomic Force Microscopy to visualize recently deposited cellulose microfibrils in the outer wall of the abaxial epidermis of sepals[28]: a nanometer-sized probe was used to scan the protoplast-facing surface of the wall sample and measure the height of contact (**Fig 1A,B**). Maps presented various orientations of microfibrils (**Fig 1A,B**). There was also a proportion of regions with only one apparent orientation (2 out of 62 for WT, 12 out of 100 for *csi1-3*), although the difference between these proportions was not significant (p-value of normal z-test = 0,08). Therefore, we developed an index to quantify to what extent the microfibrils are aligned (**Fig 1C**). Briefly, microfibrils orientation distribution was decomposed into Gaussians and the alignment index was computed as the maximum angular distance between these Gaussians. We found that cellulose microfibrils were more aligned in *csi1-3* compared to WT (means = 90 and 107° for WT and *csi1-3*, respectively; p-value of Mann-

Whitney test = 0.005). Next, we examined whether the effect of this mutation on cellulose deposition was associated with affected sepal morphogenesis.

### *csi1* sepals are shorter owing to reduced elongation rates

Because Arabidopsis sepals are curved, we used 3D confocal microscopy to quantify their shape parameters (**Fig 1D**). We found that *csi1-3* sepals were shorter compared to WT but had a similar width (**Fig 1E,F** means = 2140 and 1760µm for length and 840 and 846µm for width, for WT and csi1-3, respectively. p-value of t-test = $1\times10^{-10}$, 0.73, for length and width, respectively). This phenotype was similar for the *csi1-6* allele (**Fig S1A-C**), confirming that it is indeed the result of *CSI1* loss of function. Sepal contours (as seen from front, Figure 1D) also differed between genotypes, with for instance a narrower base for *csi1-3*. We quantified curvature and found that *csi1-3* sepals were significantly more curved compared to WT (**Fig S1E,G**). Higher anisotropy of microfibrils arrangement is usually associated with a higher cell growth anisotropy[13–15], which would be expected to yield longer sepals. Surprisingly, higher anisotropy of microfibrils arrangement in *csi1-3* is associated with shorter organs. We therefore analyzed the origin of the differences in elongation of *csi1-3* compared to WT.

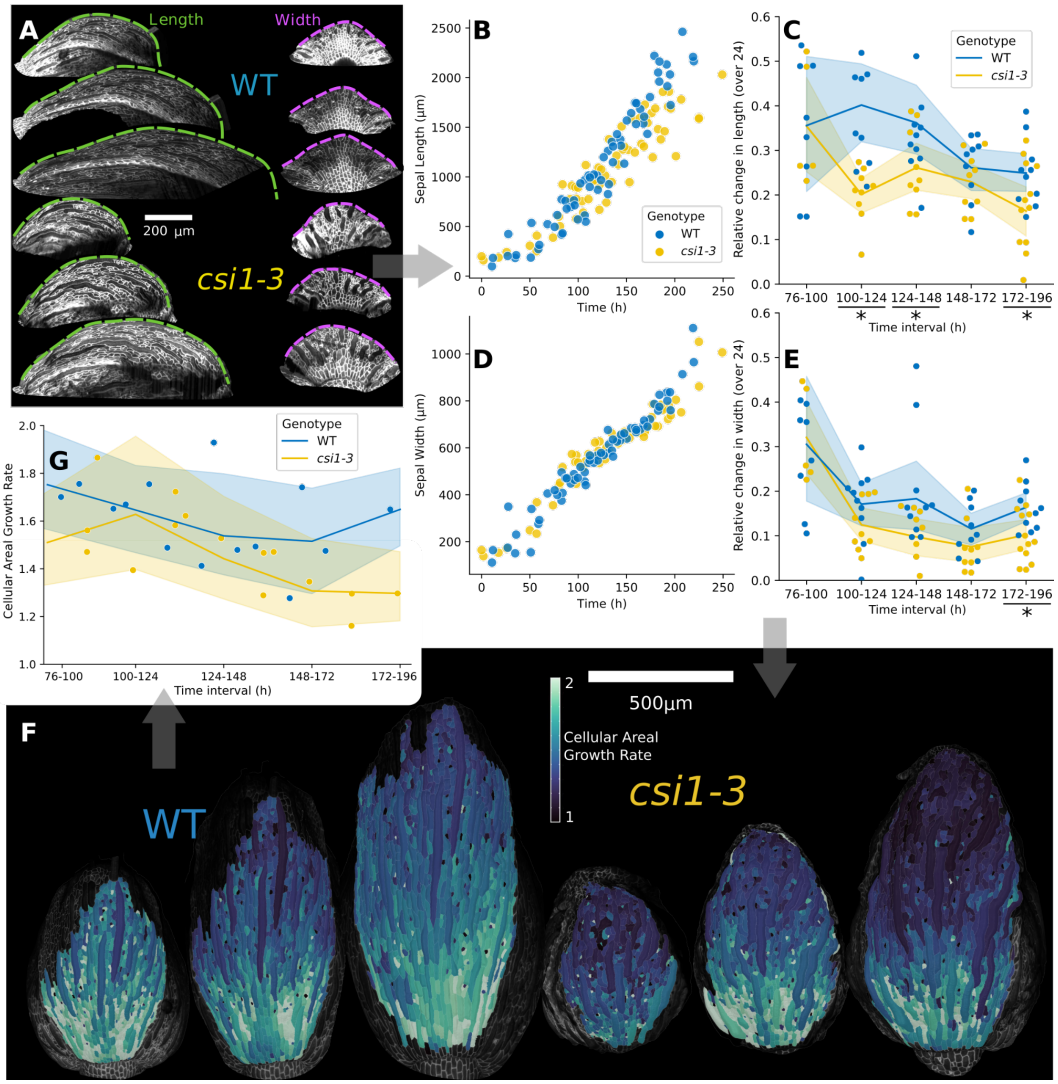


**Figure 2: *csi1* sepals have smaller elongation rates than WT at organ level, but cellular growth rates less different.**

**A.** Representative time series of sepal growth in WT (top) and *csi1-3* (bottom). Cell membranes are labeled using a *pATML1::RCI2A-mCitrine* construct. Colored dashed lines indicate measured sepal length and width. Time between acquisitions = 24h.

**B,D.** Sepal length (B) and width (D) as a function of time. Temporal sequences were registered with regard to time to define a common starting time using width, which can be mapped to developmental stages (see Supplementary Figure 2).

**C,E.** Relative growth rates in length (C) and width (E) as a function of registered time. Comparisons were made over a sliding 24h window, which corresponds to the imaging interval. Asterisks at the bottom indicate significant differences (p-value of Mann-Whitney test <0.05). WT is in blue and *csi1-3* in yellow. The lines correspond to median, the shading to the interquartile range, and the points to individual sepals.

**F.** Top view of representative time series, with cellular growth rate color-coded. Growth was calculated as the ratio of cell surface area between consecutive time points. The first sepals images are associated

184 with the 100-124h interval. Time between acquisitions = 24h. The initial time point of each series was chosen so that sepals have similar width.

186 **G.** Quantification of growth rates as a function of registered time, measured as shown in F. Time registration and symbols are the same as for panels B-E. (p-value of t-test between sepal medians: 0.1,

188 0.9, 0.5, 0.2 for time intervals 76h-100h, 100h-124h, 124h-148h, 148h-172, respectively. p-value of t-test between all cells of the sepals: $7\times10^{-31}$, $2\times10^{-7}$, $2\times10^{-14}$, $1\times10^{-57}$ for the same time intervals)

190

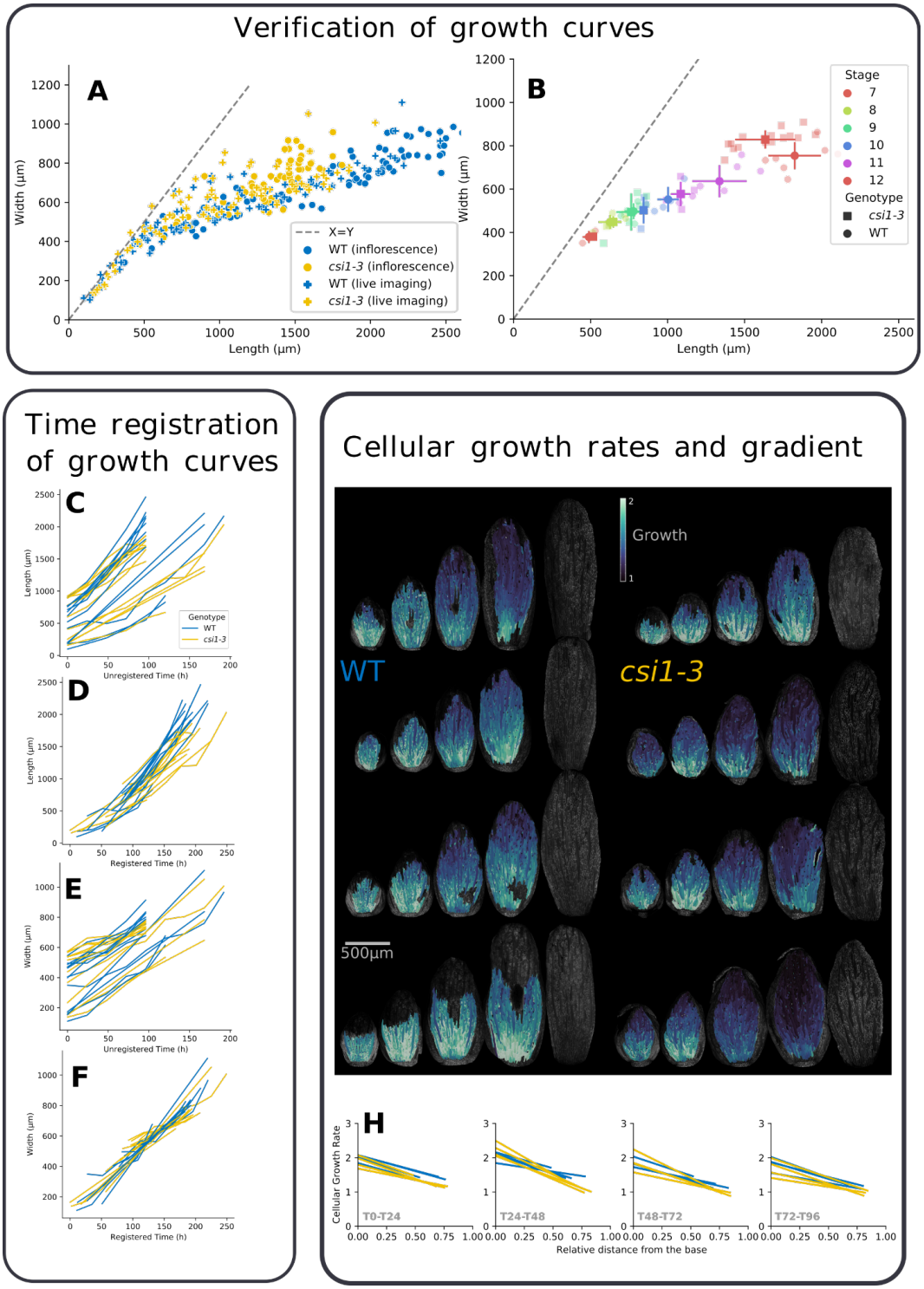

**Supplementary Figure 2:**

**A.** Comparison of growth trajectories between plants used for live imaging (individual flowers imaged live over a few days and grown in vitro following dissection) and culture room grown plants (static images from dissected inflorescences).

**B.** Comparison of developmental stage and length-width value between WT and *csi1-3* sepals. Stages used are defined in Smyth et al.[73] Note that width values of WT and *csi1-3* sepals at a given stage overlap more than length values, allowing us to use width to register time (panels C-F).

**C-F.** Growth curves from live imaging, before (C,E) and after time registration (D,F) for length (C,D) and width (E,F).

**G.** All heatmaps of cellular growth rates in area for all sepals (WT on the left, *csi1-3* on the right); sepals were imaged over 5 days, yielding 4 maps. Regions with a low quality signal were not segmented.

**H.** Growth gradients visualized for all the time points. Each line corresponds to a first degree polynomial fit between cellular growth rates and relative distance from cell to the base of the sepal. Sepal total length used here to compute the relative position was measured manually.

To understand the differences in final length between WT and *csi1-3* sepals, we considered sepal morphogenesis and performed live imaging of developing sepals (**Fig 2A**). As we used dissected inflorescences grown in vitro, we first checked whether our in vitro growth conditions produced similar organs compared to normally grown plants. We compared sepal length and width between inflorescences growing in the two conditions (**Fig S2A**). We found that sepal dimensions are similar throughout development showing that in vitro conditions do not affect sepal morphogenesis. In order to compare developmental trajectories between the two genotypes, WT and *csi1-3,* we developed a common temporal frame for all sepals. Because width is similar between WT and *csi1-3* sepals at a given developmental stage (stage 12 in **Fig 1F**; all stages in Fig S2B), we used width to shift the time of each live imaging sequence and put all sepals into the same time frame, further referred to as registered time (**Fig S2C-F**). The outcome is shown in **Fig 2B,D**, with a common initial time (0h) that corresponds to stage 5 of flower development.

We found that sepal growth can be approximately decomposed in two different phases. In the first, overall sepal growth is isotropic, with length and width increasing similarly, up to a size of about 500µm, corresponding to a time of about 75h in our registered time frame. Differences between WT and *csi1-3* are small in this isotropic growth phase. In the second phase, sepal growth is anisotropic and trajectories of WT and *csi1-3* appear to diverge (**Fig S2A**). We

quantified the rate of increase in dimensions of WT and *csi1-3* sepals during this second phase. We found no differences concerning width except for the last time interval (**Fig 2E**). Rate of increase in length is however smaller in *csi1-3* throughout development (**Fig 2C**) showing that sepals from *csi1-3* plants are shorter because they elongate less compared to the WT all along the second phase of sepal morphogenesis, and not because of an early arrest of growth.

**At cellular scale, neither growth rate nor growth anisotropy can explain differences in sepal elongation**

Next, we sought to understand the cellular basis of the differences in sepal elongation rates. We first focused on the simplest aspect of growth: cell areal growth rate. We imaged sepals in dissected inflorescences with cellular resolution, segmented and tracked over time the surface of outer epidermal cells from the times series of highest quality among those used for **Fig 2F** (N=4 for WT and for *csi1-3*). We quantified cell areal growth rate as the ratio of area between two consecutive time points (if a cell has divided, we fuse the daughter cells to compute this ratio). We found cellular growth rates slightly higher in WT compared to *csi1-3* when looking at the whole sepal, which may explain the difference in final sepal area (**Fig 2G**). We verified that the possible existence of a base-to-tip growth gradient does not affect this conclusion (**Fig S2G,H**). However, these differences in cellular growth rates cannot explain the differences in the ratio of length to width observed for mature sepals. Other cellular parameters that could explain macroscopic differences are the main direction in which cells are growing (i.e. the direction of maximal growth), and how much they grow in this direction compared to the perpendicular direction (i.e. the direction of minimal growth), which is known as cell growth anisotropy.

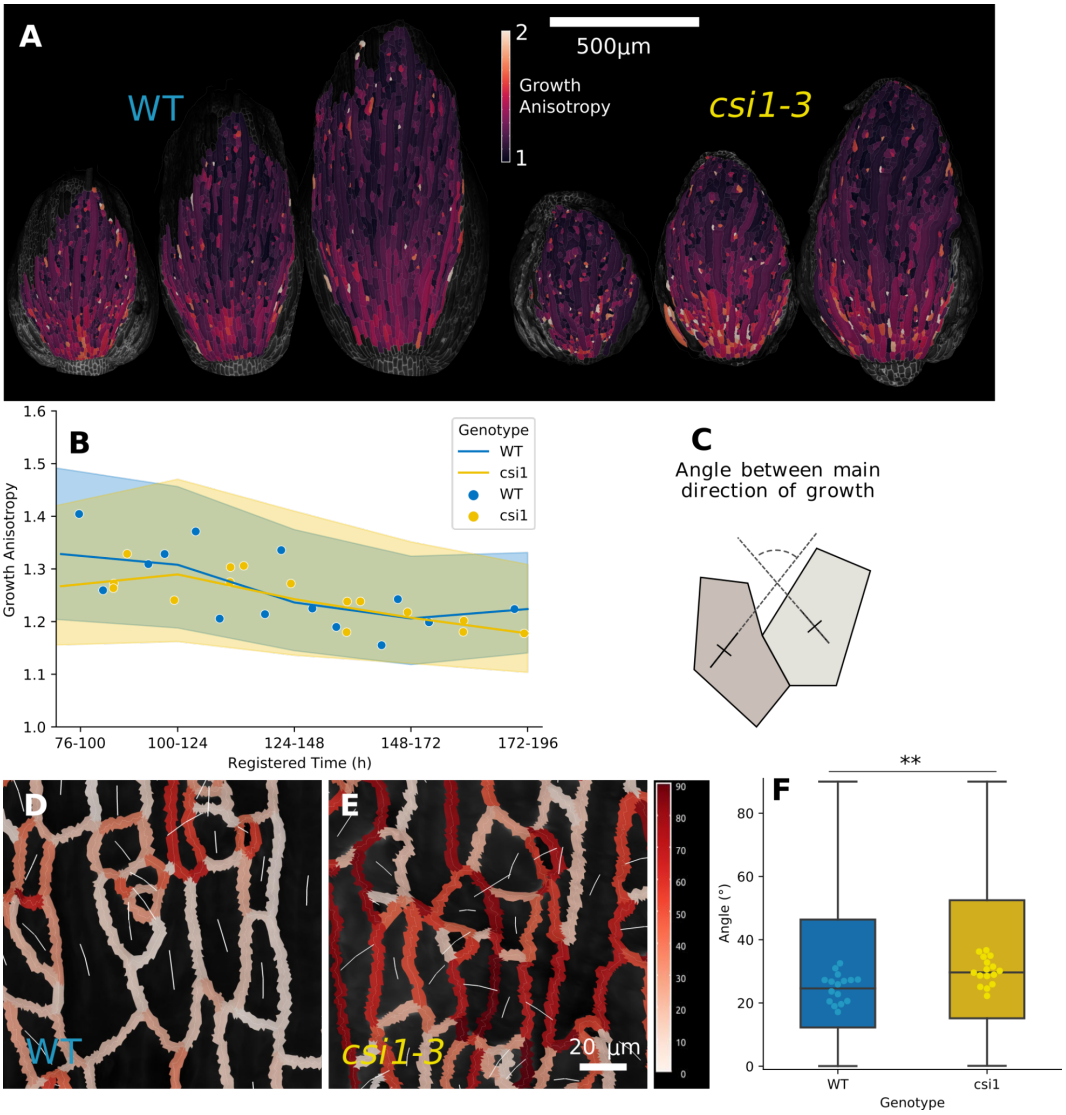


**Figure 3: Growth anisotropy is similar between *csi1* and WT, but spatial consistency of growth direction is affected in *csi1***

**A.** Representative time series, with cellular growth anisotropy color coded. Growth anisotropy was quantified on the basis of relative displacements of three-way wall junctions — a value of 1 means that growth is isotropic and the highest values of anisotropy are above 2 (the color scale was capped to 2 to avoid saturation).

**B.** Quantification of cellular growth anisotropy as a function of registered time, corresponding to all times series as in A. WT is in blue and *csi1-3* in yellow. The lines correspond to median, the shading to the interquartile range, and the points to average values for individual sepals (four series for each genotype). (p-value of t-test between sepal medians: 0.2, 0.7, 0.9, 0.7 for time intervals 76h-100h, 100h-124h, 124h-148h, 148h-172, respectively. p-value of t-test between all cells of the sepals: $8\times10^{-4}$, 0.23, 0.08, 0.02 for the same time intervals)

**C.** Schematic drawing explaining the quantification of spatial consistency of main growth direction shown in panels D and E. The angle is measured between the 3D vectors corresponding to the main growth directions of each pair of neighboring cells.

**D,E.** Representative images of main growth direction (white lines, with line length proportional to cell growth anisotropy) and of angle between growth directions of pairs of neighboring cells visualized by the color of their common anticlinal wall (the red colorbar spans angles from 0 to 90°).

**F.** Boxplots of the angle between main growth directions in neighboring cells. Box plots were constructed using all pairs of neighboring cells. Points represent the median angles for individual sepals. (Total number of pairs of cells analyzed = 30972, and 27853 for WT, *csi1-3*, respectively. p-value of t-test between every pair of cells = $10^{-88}$. p-value of t-test between the median values for individual sepals = 0.002).

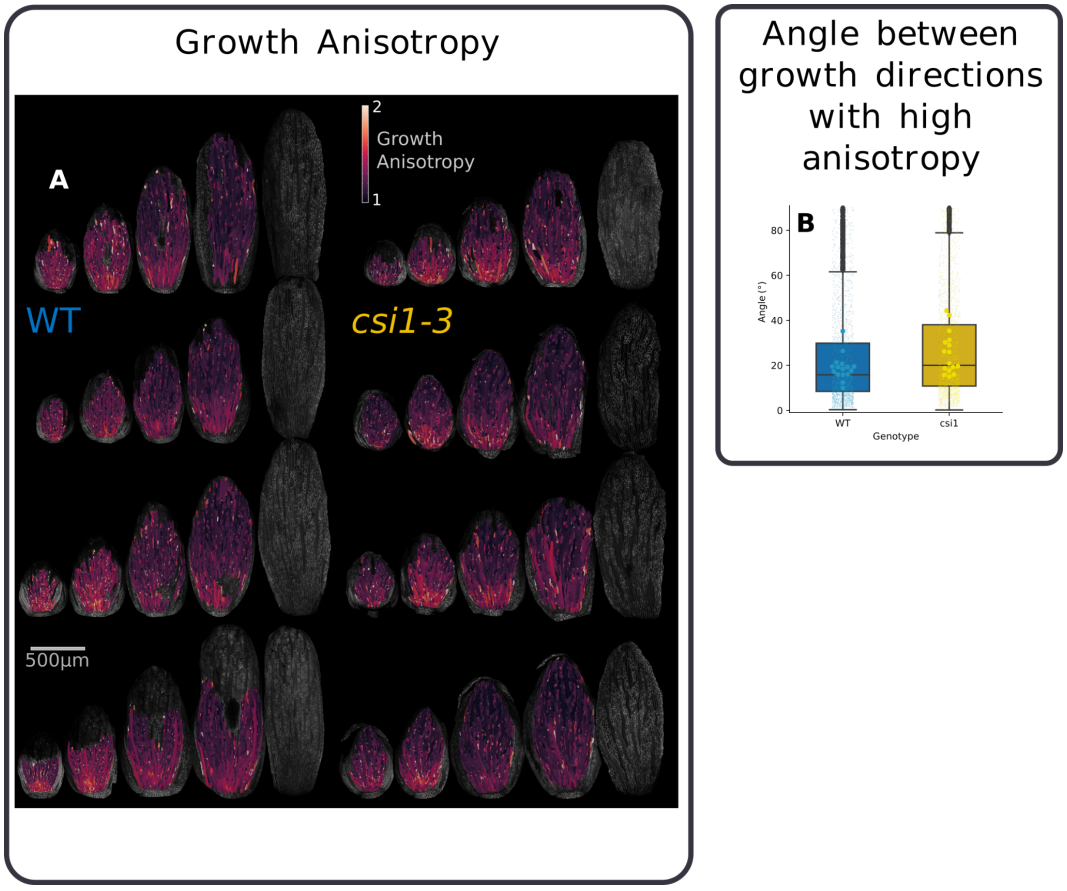


**Supplementary Figure 3**

**A.** Heatmaps of cellular growth anisotropy for all the examined sepals (WT on the left, *csi1-3* on the right); sepals were imaged over 5 days, yielding 4 maps. Zones with a low quality signal were not segmented.

**B.** Angle between main growth directions in neighboring cells with anisotropy of at least 1.4. Large dots represent the median angle for a given sepal. Small points represent individual values between pairs of cells. Box plots were constructed using all the pairs of cells. (Total number of pairs of cells analyzed = 2583, and 2285 for WT, *csi1-3*, respectively. p-value of t-test between the median values for cell pairs = $10^{-11}$. p-value of t-test between the median values for sepals = 0.03).

Using the same live imaging data, we quantified cell growth anisotropy (**Fig 3A**). We found no differences between WT and *csi1-3* (**Fig 3B**). This was unexpected considering that at organ scale sepals grow less anisotropically in *csi1*-3 than in WT. In order to find the cause of organ scale differences, we then considered a remaining cellular parameter, the main direction of cell growth.

**Spatial consistency of growth direction is lower in *csi1***

We assessed spatial consistency by measuring the angle between the directions of maximal growth of all pairs of neighboring cells (**Fig 3C,D,E**). If the angle is small, it means that the two cells grow in a similar direction. In order to assess the meaning of these values, we computed a theoretical maximum for this angle. When we assigned random orientations to cell growth on a sepal mesh, we found a median of 45° for the angle between growth directions of two cells. In live imaging data, we found that the median angle between the main growth directions of cells in *csi1-3* is higher compared to WT, 30° and 25°, respectively (**Fig 3F**). These values are smaller than 45°, which means that there is some level of spatial consistency in the two genotypes, but with higher consistency for WT. Because the definition of cell growth direction is not meaningful in the case of cells with nearly isotropic growth, we also computed the same metrics for cells with a growth anisotropy higher than a threshold of 1.4 and ended up with the same conclusion (**Fig S3A**). These results show that CSI1 plays a role in the consistency of growth direction. Cells growing in less consistent directions in *csi1-3*, compared to WT, may explain reduced elongation of *csi1-3* sepals.

An outstanding discrepancy is that cellulose appears more aligned in *csi1-3* than in wild-type in AFM maps, whereas anisotropy of cell growth is unaffected. A possible explanation could be that AFM topography only detects the most recently deposited layer of cellulose microfibrils, while all the layers of the cell wall play a role in the control of growth anisotropy. We therefore assessed cellulose alignment over the entire thickness of the cell wall using Raman microspectroscopy.

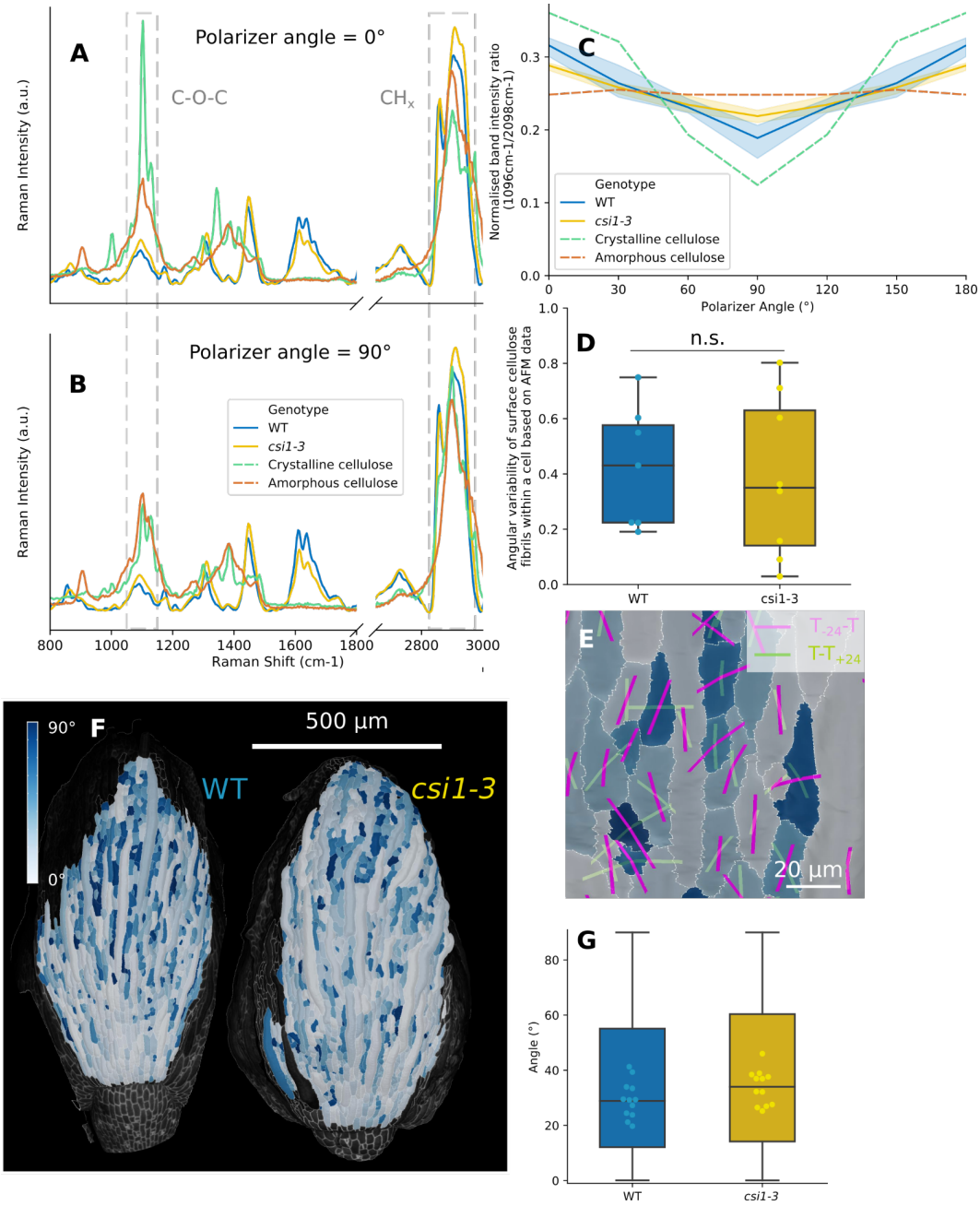


**Figure 4: Cellulose is less aligned at micrometric scale in *csi1* compared to WT, and growth direction is slightly less persistent in *csi1***

**A-B.** Representative Raman spectra of cell walls from WT and *csi1-3* sepals and purified extract of crystalline and amorphous cellulose collected at different polarization angles (here 0° is shown in panel A and 90° in panel B). Spectrum fragments include two cellulose-specific bands centered at 1096cm-1 (related to C-O-C linkage), and at 2898cm-1 (CHx, x=1,2 linkages)

**C.** Overall cellulose alignment in the outer epidermal cell walls assessed by ratio of integrated intensity changes from cellulose-specific bands accompanying polarizer angle changes in the 0-180° range. Analysis of WT and *csi1* was compared with two reference samples: crystalline and amorphous cellulose. Each ratio value was normalized by the sum of all ratios for the sample to better illustrate the relative changes between samples. The values from 120° to 180° have been duplicated from the 0° to

60° values to show periodicity. The lines correspond to median, the shading to the interquartile range for sepals. (Total number of sepals analyzed = 4 for WT and *csi1-3.* p-values of t-test for each angle between WT and *csi1-3* = 0.02, 0.70, 0.69, 0.09 for angles 0°, 30°, 60° and 90°, respectively).

**D.** Angular variability within a cell of the main cellulose microfibrils orientation on the wall surface facing the protoplast, computed on the basis of AFM maps. Angular variability is defined as the circular variance and is therefore bounded between 0 and 1. (Total number of sepals analyzed = 7 and 8, for WT and *csi1-3,* respectively. p-value of t-test between angular variability = 0.78).

**E.** Illustration of the quantification shown in F & G. Main growth directions of the cells are represented by magenta and green lines, corresponding to growth direction computed with the previous time point, and with the following, respectively. Cells are colored depending on the angle between growth directions at consecutive time intervals. Colorbar is the same as in F.

**F.** Representative maps with cell color coded depending on the angle between growth directions at consecutive time intervals.

**G.** Angle between growth directions at consecutive time intervals. Points represent the median angle for a given sepal. Box plots were constructed using all cells. (Total number of cells analyzed = 7533, and 7025 for WT, *csi1-3*, respectively. p-value of t-test between every cell = $10^{-14}$. p-value of t-test between the median values for sepals = 0.1).

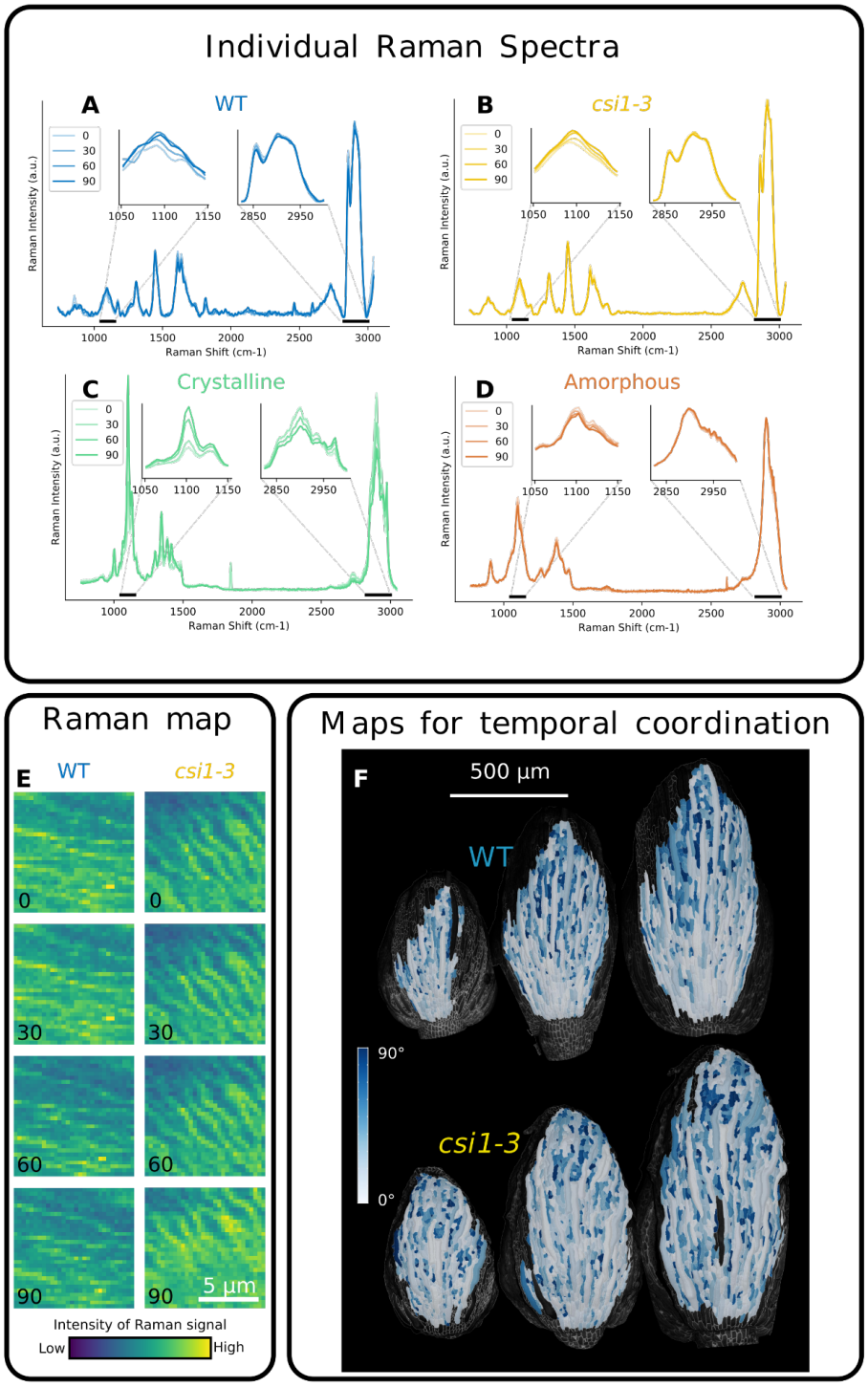


340 **Supplementary Figure 4:**

**A-D.** Examples of Raman spectra obtained for WT, *csi1-3*, crystalline cellulose and amorphous cellulose
342 at different polarization angles. Insets represent a zoom around the bands centered at 1096cm$^{-1}$ and 2898cm-1, which were considered for the main figure analysis. Differences in color intensity correspond
344 to the different angular positions of the polarizer.

**E.** Examples of Raman maps prepared on the basis of the integrated intensity over a C-O-C band at 1096cm$^{-1}$ (10µm×10µm) of WT and *csi1-3* outer wall of epidermis. Numbers at the lower left corner indicate the angle of the polarizer.

**F.** Maps of the angle between growth directions at consecutive times.

## Cellulose is less aligned at micrometric scale in *csi1* compared to WT

Polarized Raman microspectroscopy is an imaging mode that provides spatial information on the molecular structure of the cell wall, including crystallinity and, thanks to light polarization, main orientation of the functional groups of cell wall polymers[29,30]. Cellulose that forms microfibrils is an example of such polarization-sensitive polymer. Thus, to assess the arrangement of cellulose, we compared the Raman spectra of outer cell walls of *csi1-3* and WT sepal epidermis to two reference samples composed of pure crystalline cellulose or pure amorphous cellulose (**Fig 4A,B S4A,B,C,D**). We considered the integrated intensity ratio of two spectral bands: one centered at 1096cm$^{-1}$ that is related to C-O-C linkages, and the other focused at 2898cm$^{-1}$, related to C-H and H-C-H linkages. If cellulose microfibrils are aligned, the signal intensity of these two bands is anticorrelated (one is maximal while the other is minimal, at the same polarizer angle)[31]. First, we found that for the crystalline cellulose the signal intensity ratio changes dramatically when the polarizer angle changes, as expected for a highly organized material, depicting a strongly anisotropic cellulose arrangement (**Fig S4A**). We defined the 0° polarizer angle as that for which the signal of 1096cm$^{-1}$ band attains a maximum value, and 90° as an angle of the minimal signal (**Fig 4A,B, S4A,B,C,D**). Also as expected, amorphous cellulose presented no obvious maximum, but rather a constant signal intensity independent of the polarizer angle, indicating an isotropic material (**Fig 4C, S4D**). In both WT and *csi1-3* changes in the signal ratio lie between the reference samples indicating an intermediate anisotropy of cellulose microfibrils arrangement (**Fig 4C**). Furthermore, *csi1-3* cell wall is more similar to amorphous cellulose than WT cell wall (**Fig 4C**). This indicates that, at micrometric scale, the arrangement of cellulose is less anisotropic in *csi1-3* sepals. Considering that microfibrils arrangement in recently deposited wall layers in *csi1-3* is more anisotropic than in WT, we interpreted the Raman results as an indication that either microfibrils orientation varies more along the cell wall or across cell wall thickness in the mutant. To test this hypothesis, we looked at variation along the surface of the cell wall in our AFM data. For cells that had several regions that were imaged with high cellulose microfibrils alignment, we measured the main microfibrils orientation on each map and quantified the

circular variance associated with each cell (**Fig 4D**). We found no significant differences between WT and *csi1-3,* favoring the hypothesis that the differences observed between the AFM and the Raman results come from variability of cellulose microfibrils orientation across the thickness of the wall. If microfibrils orientation across the cell wall layer kept changing in *csi1*, we would expect cell growth to be less persistent over time (cells can not maintain growth direction over a long period of time).

Cell capacity to maintain a growth direction over extended periods of time likely depends on how long they are able to keep a consistent reinforcement of their cell walls (dependent on orientation of cellulose microfibrils). To quantify persistence of growth directions, we projected cell growth directions at consecutive time intervals (computed from 3 consecutive segmented images) on the image corresponding to the intermediate image, and quantified the angle between the two vectors corresponding to the main growth direction (**Fig 4E,F,G, S4F**). We found temporal variations of growth direction to be slightly higher in *csi1-3* compared to WT, with medians of 34° and 29°, respectively (see p-values in figure legend). Altogether, we concluded that CSI1 is required for temporal persistence and spatial consistency of growth direction. We further tested this conclusion by examining its potential consequences on cell arrangements and tissue mechanics in fully grown sepals.

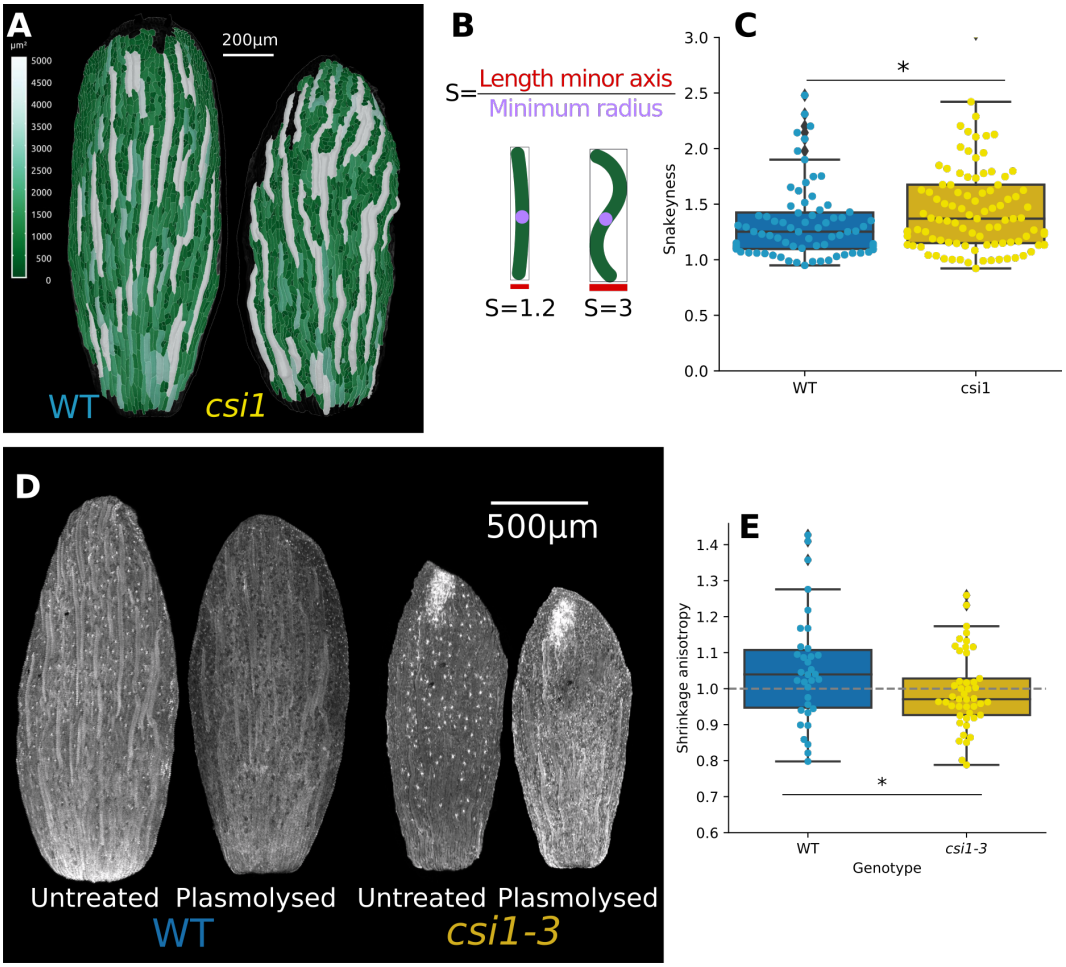


**Figure 5: In *csi1*, giant cells are snakey and sepal mechanical anisotropy is reduced**

**A.** Representative confocal images of cells of WT and *csi1-3* mature sepal. Cell area is color coded.

**B.** Illustration of the quantification of snake-y-ness.

**C.** Box plot of the quantification of cell snakeyness (Total number of cells analyzed = 75 from 4 WT sepals, 101 from 5 *csi1-3* sepals, p-value of t-test = 0.04)

**D.** Representative front view of sepals before and after plasmolysis in 0.4M NaCl for 1h.

**E.** Box plot of anisotropy of sepal shrinkage upon osmotic treatment. Points represent individual sepals (n = 34 for WT, 45 for *csi1-3* , p value of t-test = 0.04).

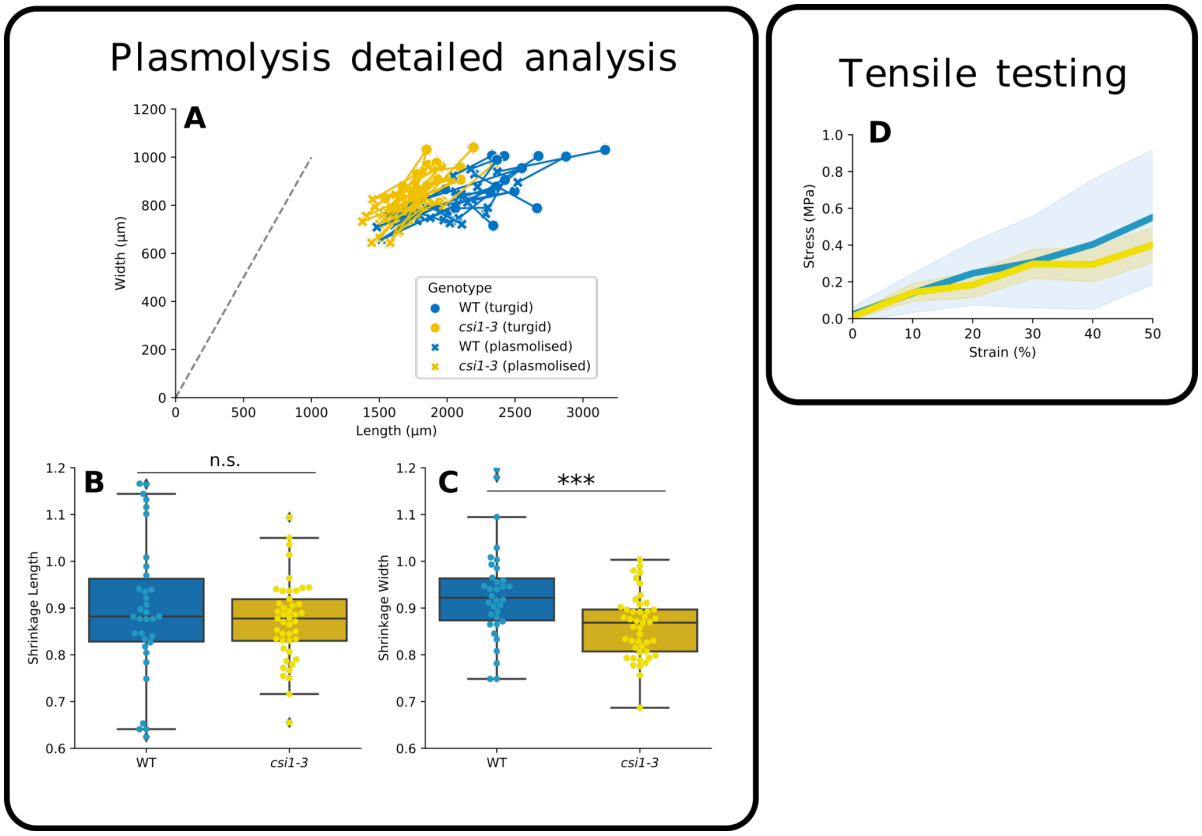


**Supplementary Figure 5:**

**A.** Representation of shrinkage in length/width coordinates. Circles correspond to sepals before osmotic treatment, crosses to after treatment. Points for each sepal are linked by a line.

**B,C.** Quantification of sepal shrinkage upon osmotic treatment for length and width, respectively (p values of t-test = 0.3 and $5\times10^{-4}$); the vertical axis indicates the ratio of dimension (length or width) after treatment to before treatment.

**D.** Stress vs. strain for sepals stretched by extensometry. WT is in blue and *csi1-3* in yellow; the lines correspond to median and the shading to the interquartile range (N=8 sepals for WT and *csi1-3*).

## Reduced spatial consistency in *csi1* is associated with snakey giant cells and reduced mechanical anisotropy at organ level

At the scale of a few cells, we expected that mechanical conflicts generated by reduced spatial consistency (differences in growth direction between neighboring cells) in *csi1-3* affects cell shapes, as cells in a tissue are tightly connected through their cell walls. To test this prediction, we used a confocal microscope to image the cells of mature (fully grown) sepals in WT and *csi1-3* (**Fig 5A**). The most striking phenotype is observed for giant cells that are approximately straight in WT and snakey in *csi1-3*. To quantify "snakeyness" we computed the ratio between

the small side of the rectangle that wraps the cell and the radius of the cell (**Fig 5B**). Cells that are straight will present similar values for these two parameters while snakey cells will have the small side of the rectangle bigger than cell radius. We found that giant cells from *csi1-3* sepals were indeed more snakey compared to WT (**Fig 5C**). Both the absence of spatial consistency and the lack of temporal persistence could explain this phenotype. Because cells are growing in more variable directions with respect to each other in *csi1-3*, cells on one side of a giant cell could grow perpendicularly to the axis of the giant cell while cells on the other side could grow parallel to this axis, leading to the snakey phenotype.

At macroscopic scale, we expected that reduced spatial consistency and temporal persistence in *csi1-3* yields less consistent orientation of cellulose microfibrils along mature sepal than in WT and thus decreases the mechanical anisotropy of the whole sepal. To quantify sepal mechanical anisotropy, we assessed shrinkage of the whole sepal upon osmotic treatment[25] and determined sepal shape parameters with our imaging pipeline (**Fig 5D**). We measured shrinkage on a length-width axis and shrinkage anisotropy defined as the ratio of shrinkage in length to shrinkage in width (**Fig S5A,B,C**). We found significant differences in the shrinkage in width (**Fig S5C**) but no differences in the shrinkage in length (**Fig S5B**). We performed independent measurements of the mechanical properties in length via tensile testing[32], which agreed with the results of osmotic treatments for the same magnitudes of strain (**Fig S5D**). Consequently, *csi1-3* shrinks less anisotropically than WT (**Fig 5E**), in agreement with expectations.

## Discussion

We investigated the link between sepal morphogenesis and the guidance of cellulose synthases by microtubules using the *csi1* mutant. We found that, despite increased anisotropic arrangement of recently deposited cellulose microfibrils, sepals are less elongated in the *csi1* mutant. This could not be ascribed to cell growth anisotropy which is comparable between *csi1* and wild-type (WT). However, we found that growth directions in *csi1* cells are temporally slightly less persistent and spatially less consistent than in WT. This lack of consistency in *csi1* explains shorter sepals and leads to snakey cells and to mechanically less anisotropic organs.

While cellulose microfibrils in *csi1* hypocotyls appear highly aligned[33], we observed that they were not as strongly aligned in *csi1* sepals (Figure 1). In the absence of guidance by cortical microtubules, cellulose synthases (CESA) were observed to either follow previous microfibrils or to move along a straight line[24,34]. The relative weight of these modes of CESA motion may

462 depend on the organ, potentially explaining differences in the *csi1* phenotype between hypocotyl and sepal, possibly due to different proteomes between the two types of organs[35]. In
464 addition, other matrix polysaccharides are also likely involved in guidance of CESA[36–38].

466 Here, we found that guidance of CESA by microtubules does not influence the degree of growth anisotropy but rather growth direction. Disruption of guidance increased spatial and temporal
468 variations of growth direction. As proposed in[24], synthesis along previous fibrils could provide memory of the wall state and help resisting perturbations by forming a template for when
470 cellulose synthesis starts again[18,39,40], whereas guidance by microtubules provides the control needed for morphogenetic events[41] or to keep track of an organ level direction. Similar ideas
472 might extend to extracellular matrix in animals, with regimes in which direction of matrix synthesis is steady[42], and regimes associated with morphogenetic events[43,44].
474

How cells in a tissue all align in the same direction has been partly elucidated in animals. Cell
476 polarity may be oriented by an instructive signal formed by a large-scale gradient or by polarity of neighboring cells via surface proteins[45,46]. Similar ideas have been proposed for plants[45,47],
478 in which the coupling between polarities of neighboring cells would involve a large set of actors[48]. Although CSI1 could have other functions than guidance, our work suggests that CSI1
480 contributes to growth coordination by translating cell polarity into growth direction, through CESA guidance by microtubules. Whereas we did not observe any twisting phenotype in sepal,
482 *csi1* mutation leads to twisting of other organs such as the leaf[49,50], hypocotyl or shoot[51]. Instead, *csi1* sepal featured snakey cells. Interestingly, Drosophila mutant oocytes with deficient
484 polarity also show snakey cell files[52]. Organ twisting and cell snakyness could be interpreted as impaired orientation by large-scale instructive signals.
486

Plant hormones are good candidates for such organ-level signals. In particular, auxin presents
488 gradients and its movement is polarly facilitated by PIN proteins[53], notably in lateral organs such as the leaf[54]. PIN1 polarity is coupled with microtubule orientation[55], supporting a
490 potential role for auxin in orienting cell growth direction. Indeed, sepals with affected auxin polarity displayed reduced length[56], although it is unclear whether this involves lack of
492 consistency of growth direction. Mechanical stress is another potential organ-level instructive signal, and studies in animals suggest that it may orient cell polarity[57,58]. In plants, microtubules
494 align with maximal stress direction[59,60], which explains the transverse orientations of microtubules seen in sepal[61].

Here, we propose that the main role in organ morphogenesis of guidance of CESA by microtubules is to enable growth direction to follow large scale signals. Interestingly, chemical perturbation of the consistency of cortical microtubules orientation in the root reduces overall organ elongation[62]. We extend these results by describing consistency of cell growth direction and pinpoint the role of CSI1 in consistency. It would be worthwhile to examine whether similar ideas apply to elongation of animal organs. For instance, cell division is oriented during limb bud elongation in the mouse[63], but the spatial consistency of divisions has not been assessed. Altogether, our work illustrates the potential in deciphering the basis of the robustness of morphogenesis by assessing spatial and temporal variability of growth and of its regulators, from subcellular to organ scale.

**Acknowledgements**

We acknowledge the contribution of SFR Biosciences (UAR3444/CNRS, US8/Inserm, ENS de Lyon, UCBL) imaging facility, PLATIM / Lymic. We acknowledge A. Lacroix, J. Berger, P. Bolland, H. Leyral and I. Desbouchages for assistance with plant growth and logistics. We thank Mathilde Dumond and Justine Chabredier for the initial exploration of the *csi1* phenotype. We thank Olivier Hamant, Adrienne Roeder, and Christophe Tréhin for fruitful discussions and suggestions. We thank Yoshiharu Nishiyama for the generous gift of reference cellulose samples. This work was funded by the French National Research Agency (ANR, grant ANR-17-CAPS-0002-01 V-Morph, to AB and OH) the National Science Centre, Poland (NCN, grant 2017/24/Z/NZ3/00548, to DK), and the German Research Foundation (DFG, grant 355722357, to RS) through a European ERA-NET Coordinating Action in Plant Sciences (ERA-CAPS) grant. This work was also directly funded by the French National Research Agency (ANR, grant ANR-17-CE20-0023-02 WALLMIME, to AB) and by the National Science Centre, Poland (SHENG1 grant 2018/30/Q/00189, to DBW).

**Author contributions**

Conceptualization: CM, FM, DK, AB

Methodology: CM, JS, DBW, MM, MD, AF, EW, DK, AB

Software: CM, JS, RS, DK

Validation: CM, JS, MM, MD

Formal Analysis: CM, JS, MM, MD, AF, RS, DK

Investigation: CM, JS, DBW, MM, MD, RW, DK

Data Curation: CM, JS, DBW, MM, MD, DK

Writing - Original Draft Preparation: CM, FM, AB

Writing - Review & Editing: CM, JS, MD, RS, FM, DK, AB

Visualization: CM

Supervision: RS, FM, DK, AB

Project Administration: RS, DK, AB

Funding Acquisition: RS, DK, AB

## Materials and methods

### Experimental model and subject details

*Arabidopsis thaliana* plant lines used for live imaging and analysis of mature sepal cell shape were pAR169 (ATML1p::mCirtrine-RCI2A,[27]) and *csi1-3* x pAR169. In all other cases the plants used were Col-0, *csi1-3* (SALK_138584,[64]), *csi1-6* (SALK_115451,[64]). All lines had a Col-0 background. Plants were grown on soil at 22°C in culture rooms with long day conditions (16 h light/8 h darkness). For in vivo imaging, inflorescences were cut off from the plants, dissected up to the desired bud (all buds used in this study were comprised between the 10th and 20th organ initiated along the inflorescence [25]) and grown into apex culture medium plates[65] supplemented by 0.1% V/V plant preservative mixture (PPM; Plant Cell Tech). Plates were then stored in growth cabinets with the same lighting/temperature conditions as in culture rooms.

### Methods Details

*Confocal imaging and analysis*

Whole sepal images were collected using a LSM700 confocal microscope (Zeiss, Germany) equipped with a 5x air objective (NA = 0.25). Propidium iodide (PI) was excited using a 555 nm laser and the emitted light filtered through a 560-630 band pass filter.

Live-imaging images were collected using a SP8 confocal microscope (Leica Microsystems, Germany) equipped with a 25× long-distance water objective (NA = 0.95). mCitrine was excited using a 514 nm laser and the emitted light filtered through a 520-550nm band pass filter.

Samples used for whole sepal measurements were stained in PI at 100µM final concentration in water for 15 minutes prior to imaging. Sepals used for osmotic treatments were then plasmolysed for 1h in 0.4M NaCl solution supplemented with PI at 100µM.

Whole sepal measurements were performed following[66]. Quantification of macroscopic growth rates was done by measuring manually sepal curved length and width using oriented images in ImageJ.

Live imaging data was analyzed using MorphoGraphX[67], which included segmentation, lineage tracking and computation of the cell areas and principal direction of growth. Principal growth directions of each cell were computed based on the relative displacement of three-way cell junctions between consecutive imaging time points. Growth anisotropy was then calculated as the ratio between magnitudes associated with the maximum and minimum principal directions of growth.

*Atomic Force Microscopy (AFM) and quantification of cellulose microfibrils arrangement on protoplast-facing wall surface*

Samples of recently formed cell wall surface (i.e. the protoplast-facing surface) were prepared for AFM measurements using a modified protocol of Wuyts et al.[68] Briefly, the sepals were plasmolysed in 0.4 M NaCl for 10 min and fixed in 70% ethanol (first kept under vacuum for 1 h at room temperature, next fixed for at least 24 h at 4°C). Afterwards they were treated with absolute chloroform for 10 min (to remove membranes and cuticle), rehydrated in decreasing ethanol series (70%, 50%, 30%) followed by deionized water (5 min in each medium), placed in protoplast lysis buffer of sodium dodecyl sulfate and sodium hydroxide (1% SDS in 0.2M NaOH) for 3 h, treated with 0.01% α-amylase (Sigma-Aldrich; from *Bacillus licheniformis*) in PBS (Phosphate Buffered Saline) (pH 7.0) in 37°C overnight (to remove residual starch), moved to over-saturated water solution of chloral hydrate (200 g / 50 ml) for 4 h (to remove protoplast remnants), and rinsed in water (3 x 15 min). Superficial cell walls of the abaxial epidermis were then gently peeled off from the sepal and placed on the glass slide such that the protoplast facing wall surface was exposed. In order to better visualize the cellulose microfibrils in some samples, pectins were removed by treatment with 2% pectinase (Serva, Heidelberg, FRG; from *Aspergillus niger*) in sodium-phosphate buffer (pH 5.7) at room temperature for 30 min, or the buffer alone. The samples were then rinsed in water and dried at room temperature, during which the wall became attached to the glass slide by adhesion.

Atomic Force Microscopy (AFM) measurements were performed with a NanoWizard®3 BioScience (JPK Instruments, Berlin, Germany) operating in intermittent contact mode, using

HQ:NSC15 rectangular Si cantilevers (MicroMasch, Estonia) with spring constant specified as 40 N/m, cantilever resonant frequency of about 325 kHz, and tip radius 8 nm. All scans were conducted in air in laboratory conditions (22°C, constant humidity of 45%). Images were obtained using the JPK Data Processing software (JPK Instruments).

Anisotropy of cellulose microfibrils arrangement was assessed for square regions (400 nm x 400 nm) with distinct microfibrils chosen from measured height images of 2 µm x 2 µm AFM scans (2-4 regions per scan). Histogram of microfibrils orientation was obtained for each region using Directionality tool (https://imagej.github.io/plugins/directionality) of Fiji (Fourier components method). In the Directionality tool, alignment is assessed for a single curve fitted to the highest peak while in most cell wall regions the distribution of microfibrils orientation was multimodal. Thus, we a developed a bespoke protocol written in Matlab (Mathworks, Nattick, MA, USA) to quantify microfibrils arrangement using the following steps: (i) smooth the histogram by a moving average; (ii) obtain a series of least square approximations of the histogram by a sum of an increasing number of Gaussian models (up to 8); (iii) choose the approximation with the lowest number of Gaussians with adjusted $R^2$>0.94; (iv) exclude Gaussians with half-width bigger than 180°; (v) concatenate Gaussians with peaks separated by less than 10°; (vi) exclude Gaussians with height smaller than ¼ of the highest peak; (vii) compute the alignment index as the maximal angular distance between the remaining Gaussian peaks.

We examined both giant and non-giant epidermal cells of sepals (5 sepals in WT; 6 in *csi1-3*) from stage 12 flowers. In WT we obtained 16 AFM maps from 9 cells, in *csi1-3* - 32 maps from 14 cells.

Angular variability was computed on cells on which at least three AFM regions with alignment index greater than 140° were obtained. Angles were periodised and circular variability was measured using the asotropy package[69,70].

*Raman spectroscopy*

Sample preparation for Raman microspectroscopy followed the AFM protocol up to the treatment with chloral hydrate and rinsing in water [68]. Such prepared sepals were put on glass slides (1 mm thick), immersed in pure deionized water to preserve environmental conditions, and covered by $CaF_2$ 0.15-0.18 mm thick coverslips (CAMS1602, Laser Optex).

Raman data were collected using WITec confocal Raman microscope CRM alpha 300R, equipped with an air-cooled solid-state laser ($\lambda$ = 532 nm), an thermoelectrically cooled CCD camera, and Zeiss C-Apochromat (100x/1.25 NA) water immersion objective. The excitation

laser radiation was coupled to the microscope through a single-mode optical fiber (50 µm diameter). Raman scattered light was focused onto a multi-mode fiber (50 µm diameter) and monochromator with a 600 line $mm^{-1}$ grating. The spectrometer monochromator was calibrated using the emission of a Ne lamp, while the signal of a silicon plate (520.7 $cm^{-1}$) was used for checking beam alignment.

Surface Raman imaging was applied to differentiate the signal of the cuticular ridges and cell wall. Data were collected in a central fragment of the cell in a 10 µm×10 µm area using 30 × 30 pixels (=900 spectra) and an integration time of 40 ms per spectrum. The precision of the horizontal movement of the sample during measurements was ± 0.2 µm. The lateral resolution (LR) was estimated according to the Rayleigh criterion LR = 0.61λ/NA as LR = 427 nm. All spectra obtained during Raman imaging were collected in the 120 - 4000 $cm^{-1}$ range with a resolution of 3 $cm^{-1}$ and at 30 mW on the sample.

The output data were processed by performing a baseline correction using an autopolynomial function of degree 3, submitted to an automatic cosmic rays removal procedure by comparing each pixel (i.e. each CCD count value at each wavenumber) to its adjacent pixels and finally smoothed by Savitzky–Golay filter. Chemical images were generated using cluster analysis (CA). *K*-means approach with the Manhattan distance for all Raman imaging maps was carried out to distinguish signal of cuticular ridges and cell wall. Every spectrum obtained from the clustering analysis was normalized by dividing by its total area using WITec Project Five Plus software. The procedure was repeated for ten non-giant pavement cells located in the basal half of different sepals.

Every time data were gathered for 13 consecutive orientations of the polarization plane (the angular range 0-180°), each rotated by 15°. From such obtained set of 13 averaged spectra after the *K*-means cluster analysis, the spectrum with maximal signal intensity of the C-O-C band (1096 $cm^{-1}$) was chosen to represent angular position 0°, while the other spectra represent angle-dependent integrated intensity alteration with minimum at 90°. Once positions of the two angular extrema were recognized, the 4 spectra (every 30° from 0° to 90°) were used for further analysis. For each spectrum the spectral parameters like band position, full width at half maximum, intensity and integrated intensity were determined by deconvolution of the spectra through the peak fitting procedure facilitated by GRAMS\AI 9.2 software. For each spectrum, the Voigt function with the minimum number of the components was used to reproduce the experimentally observed band arrangement. The applied procedure allows one to separate cellulose-specific bands, e.g. 1096 $cm^{-1}$ (C-O-C) and 2898 $cm^{-1}$ (CHx, x=1,2) from non-cellulose bands originating from other polysaccharides present in the cell wall. Finally, the ratio

of integrated intensity around the C-O-C and CHx bands was calculated to follow the angle-dependent character of the sample and estimate the extent of cellulose microfibrils ordering. The ratio of integrated intensity values estimated for those two regions was calculated for different polarizer angles (every 30° from 0° to 90°) and normalized by the sum of the four values.

Data from WT and *csi1-3* mutant were compared with purified reference samples of crystalline *(Halocynthia roretzi)* and amorphous (DMAc/LiCl) cellulose[71].

*Extensometry*

Sepal extensometry and analysis was performed according to Majda et al.[32]

*Quantifications and Statistical Analysis*

Analysis and statistical testing were performed with custom made python scripts. Statistical testing was performed using the scipy.stats library[72].

To obtain a default value of spatial consistency, we computed the median angle between neighboring cells in a sepal, ascribing a random orientation to each cell. Indeed, the maximal angle between two cells is 90°, but three neighboring cells cannot all be oriented at 90° to each other. Here, we used one example of segmented sepal mesh and we replaced growth direction with a random vector that is tangential to the surface of the epidermis because we are only considering growth of the sepal outer surface. In practice, the random vector was drawn on the plane best-fitting centroids of neighboring cells. We then applied the same pipeline used for the quantification of spatial consistency of growth direction.

## Data and Code Availability

All data and scripts will be made available with the final version of the article.

## References

1. Rauzi, M., Verant, P., Lecuit, T., and Lenne, P.-F. (2008). Nature and anisotropy of cortical forces orienting Drosophila tissue morphogenesis. Nat. Cell Biol. *10*, 1401–1410.

2. Bertet, C., Sulak, L., and Lecuit, T. (2004). Myosin-dependent junction remodelling controls planar cell intercalation and axis elongation. Nature *429*, 667–671.

3. Umeda, A., and Amako, K. (1983). Growth of the Surface of Corynebacterium diphtheriae. Microbiol. Immunol. *27*, 663–671.

4. Peaucelle, A., Wightman, R., and Höfte, H. (2015). The Control of Growth Symmetry Breaking in the Arabidopsis Hypocotyl. Curr. Biol. CB *25*, 1746–1752.

5. Bou Daher, F., Chen, Y., Bozorg, B., Clough, J., Jönsson, H., and Braybrook, S.A. (2018). Anisotropic growth is achieved through the additive mechanical effect of material anisotropy and elastic asymmetry. eLife *7*, e38161.

6. Singh, A., Saha, T., Begemann, I., Ricker, A., Nüsse, H., Thorn-Seshold, O., Klingauf, J., Galic, M., and Matis, M. (2018). Polarized microtubule dynamics directs cell mechanics and coordinates forces during epithelial morphogenesis. Nat. Cell Biol. *20*, 1126–1133.

7. Haigo, S.L., and Bilder, D. (2011). Global Tissue Revolutions in a Morphogenetic Movement Controlling Elongation. Science *331*, 1071–1074.

8. Isabella, A.J., and Horne-Badovinac, S. (2016). Rab10-Mediated Secretion Synergizes with Tissue Movement to Build a Polarized Basement Membrane Architecture for Organ Morphogenesis. Dev. Cell *38*, 47–60.

9. Zajac, A.L., and Horne-Badovinac, S. (2022). Kinesin-directed secretion of basement membrane proteins to a subdomain of the basolateral surface in Drosophila epithelial cells. Curr. Biol. *32*, 735-748.e10.

10. White, C.L., and Gober, J.W. (2012). MreB: pilot or passenger of cell wall synthesis? Trends Microbiol. *20*, 74–79.

11. Shi, H., Bratton, B.P., Gitai, Z., and Huang, K.C. (2018). How to Build a Bacterial Cell: MreB as the Foreman of E. coli Construction. Cell *172*, 1294–1305.

12. Chlasta, J., Milani, P., Runel, G., Duteyrat, J.-L., Arias, L., Lamiré, L.-A., Boudaoud, A., and Grammont, M. (2017). Variations in basement membrane mechanics are linked to epithelial morphogenesis. Development *144*, 4350–4362.

13. Green, P.B. (1962). Mechanism for Plant Cellular Morphogenesis. Science *138*, 1404–1405.

14. Suslov, D., and Verbelen, J.-P. (2006). Cellulose orientation determines mechanical anisotropy in onion epidermis cell walls. J. Exp. Bot. *57*, 2183–2192.

15. Baskin, T.I. (2005). Anisotropic expansion of the plant cell wall. Annu. Rev. Cell Dev. Biol. *21*, 203–222.

16. Mansoori, N., Timmers, J., Desprez, T., Kamei, C.L.A., Dees, D.C.T., Vincken, J.-P.,

Visser, R.G.F., Höfte, H., Vernhettes, S., and Trindade, L.M. (2014). KORRIGAN1 Interacts Specifically with Integral Components of the Cellulose Synthase Machinery. PLOS ONE *9*, e112387.

17. Robert, S., Bichet, A., Grandjean, O., Kierzkowski, D., Satiat-Jeunemaître, B., Pelletier, S., Hauser, M.-T., Höfte, H., and Vernhettes, S. (2005). An Arabidopsis Endo-1,4-β-d-Glucanase Involved in Cellulose Synthesis Undergoes Regulated Intracellular Cycling[W]. Plant Cell *17*, 3378–3389.

18. Endler, A., Kesten, C., Schneider, R., Zhang, Y., Ivakov, A., Froehlich, A., Funke, N., and Persson, S. (2015). A Mechanism for Sustained Cellulose Synthesis during Salt Stress. Cell *162*, 1353–1364.

19. Gu, Y., Kaplinsky, N., Bringmann, M., Cobb, A., Carroll, A., Sampathkumar, A., Baskin, T.I., Persson, S., and Somerville, C.R. (2010). Identification of a cellulose synthase-associated protein required for cellulose biosynthesis. Proc. Natl. Acad. Sci. U. S. A. *107*, 12866–12871.

20. Bringmann, M., Li, E., Sampathkumar, A., Kocabek, T., Hauser, M.-T., and Persson, S. (2012). POM-POM2/CELLULOSE SYNTHASE INTERACTING1 Is Essential for the Functional Association of Cellulose Synthase and Microtubules in Arabidopsis. Plant Cell *24*, 163–177.

21. Li, S., Lei, L., Somerville, C.R., and Gu, Y. (2012). Cellulose synthase interactive protein 1 (CSI1) links microtubules and cellulose synthase complexes. Proc. Natl. Acad. Sci. *109*, 185–190.

22. Lei, L., Li, S., Du, J., Bashline, L., and Gu, Y. (2013). CELLULOSE SYNTHASE INTERACTIVE3 Regulates Cellulose Biosynthesis in Both a Microtubule-Dependent and Microtubule-Independent Manner in Arabidopsis[C][W]. Plant Cell *25*, 4912–4923.

23. Xin, X., Lei, L., Zheng, Y., Zhang, T., Pingali, S.V., O'Neill, H., Cosgrove, D., Li, S., and Gu, Y. (2019). CELLULOSE SYNTHASE INTERACTIVE1- and Microtubule-Dependent Cell Wall Architecture Is Required for Acid Growth in Arabidopsis Hypocotyls (Plant Biology).

24. Chan, J., and Coen, E. (2020). Interaction between Autonomous and Microtubule Guidance Systems Controls Cellulose Synthase Trajectories. Curr. Biol. *30*, 941-947.e2.

25. Hong, L., Dumond, M., Tsugawa, S., Sapala, A., Routier-Kierzkowska, A.-L., Zhou, Y., Chen, C., Kiss, A., Zhu, M., Hamant, O., et al. (2016). Variable Cell Growth Yields Reproducible Organ Development through Spatiotemporal Averaging. Dev. Cell *38*, 15–32.

26. Meyer, H.M., Teles, J., Formosa-Jordan, P., Refahi, Y., San-Bento, R., Ingram, G.,

Jönsson, H., Locke, J.C.W., and Roeder, A.H.K. (2017). Fluctuations of the transcription factor ATML1 generate the pattern of giant cells in the Arabidopsis sepal. eLife *6*, e19131.

27. Roeder, A.H.K., Chickarmane, V., Cunha, A., Obara, B., Manjunath, B.S., and Meyerowitz, E.M. (2010). Variability in the Control of Cell Division Underlies Sepal Epidermal Patterning in Arabidopsis thaliana. PLoS Biol. *8*, e1000367.

28. Hanley, S.J., Giasson, J., Revol, J.-F., and Gray, D.G. (1992). Atomic force microscopy of cellulose microfibrils: comparison with transmission electron microscopy. Polymer *33*, 4639–4642.

29. Gierlinger, N., Luss, S., König, C., Konnerth, J., Eder, M., and Fratzl, P. (2010). Cellulose microfibril orientation of Picea abies and its variability at the micron-level determined by Raman imaging. J. Exp. Bot. *61*, 587–595.

30. Borowska-Wykręt, D., and Dulski, M. (2019). Raman Spectroscopy in Nonwoody Plants. In Plant Cell Morphogenesis: Methods and Protocols Methods in Molecular Biology., F. Cvrčková and V. Žárský, eds. (Springer), pp. 83–107.

31. Gierlinger, N., Reisecker, C., Hild, S., and Gamsjaeger, S. (2013). CHAPTER 7:Raman Microscopy: Insights into the Chemistry and Structure of Biological Materials. In Materials Design Inspired by Nature, pp. 151–179.

32. Majda, M., Trozzi, N., Mosca, G., and Smith, R.S. (2022). How Cell Geometry and Cellular Patterning Influence Tissue Stiffness. Int. J. Mol. Sci. *23*, 5651.

33. Xin, X., Lei, L., Zheng, Y., Zhang, T., Pingali, S.V., O'Neill, H., Cosgrove, D.J., Li, S., and Gu, Y. (2020). Cellulose synthase interactive1- and microtubule-dependent cell wall architecture is required for acid growth in Arabidopsis hypocotyls. J. Exp. Bot. *71*, 2982–2994.

34. Duncombe, S.G., Chethan, S.G., and Anderson, C.T. (2022). Super-resolution imaging illuminates new dynamic behaviors of cellulose synthase. Plant Cell *34*, 273–286.

35. Mergner, J., Frejno, M., List, M., Papacek, M., Chen, X., Chaudhary, A., Samaras, P., Richter, S., Shikata, H., Messerer, M., et al. (2020). Mass-spectrometry-based draft of the Arabidopsis proteome. Nature *579*, 409–414.

36. Yoneda, A., Higaki, T., Kutsuna, N., Kondo, Y., Osada, H., Hasezawa, S., and Matsui, M. (2007). Chemical Genetic Screening Identifies a Novel Inhibitor of Parallel Alignment of Cortical Microtubules and Cellulose Microfibrils. Plant Cell Physiol. *48*, 1393–1403.

37. Yoneda, A., Ito, T., Higaki, T., Kutsuna, N., Saito, T., Ishimizu, T., Osada, H., Hasezawa, S., Matsui, M., and Demura, T. (2010). Cobtorin target analysis reveals that pectin functions in the deposition of cellulose microfibrils in parallel with cortical microtubules.

Plant J. *64*, 657–667.

38. Xiao, C., Zhang, T., Zheng, Y., Cosgrove, D.J., and Anderson, C.T. (2016). Xyloglucan Deficiency Disrupts Microtubule Stability and Cellulose Biosynthesis in Arabidopsis, Altering Cell Growth and Morphogenesis1[OPEN]. Plant Physiol. *170*, 234–249.

39. Himmelspach, R., Williamson, R.E., and Wasteneys, G.O. (2003). Cellulose microfibril alignment recovers from DCB-induced disruption despite microtubule disorganization. Plant J. *36*, 565–575.

40. Liu, Z., Schneider, R., Kesten, C., Zhang, Y., Somssich, M., Zhang, Y., Fernie, A.R., and Persson, S. (2016). Cellulose-Microtubule Uncoupling Proteins Prevent Lateral Displacement of Microtubules during Cellulose Synthesis in Arabidopsis. Dev. Cell *38*, 305–315.

41. Sassi, M., Ali, O., Boudon, F., Cloarec, G., Abad, U., Cellier, C., Chen, X., Gilles, B., Milani, P., Friml, J., et al. (2014). An Auxin-Mediated Shift toward Growth Isotropy Promotes Organ Formation at the Shoot Meristem in Arabidopsis. Curr. Biol. *24*, 2335–2342.

42. Matsubayashi, Y., Sánchez-Sánchez, B.J., Marcotti, S., Serna-Morales, E., Dragu, A., Díaz-de-la-Loza, M.-C., Vizcay-Barrena, G., Fleck, R.A., and Stramer, B.M. (2020). Rapid Homeostatic Turnover of Embryonic ECM during Tissue Morphogenesis. Dev. Cell *54*, 33-42.e9.

43. Proag, A., Monier, B., and Suzanne, M. (2019). Physical and functional cell-matrix uncoupling in a developing tissue under tension. Development *146*, dev172577.

44. Loganathan, R., Potetz, B.R., Rongish, B.J., and Little, C.D. (2012). Spatial Anisotropies and Temporal Fluctuations in Extracellular Matrix Network Texture during Early Embryogenesis. PLOS ONE *7*, e38266.

45. Abley, K., De Reuille, P.B., Strutt, D., Bangham, A., Prusinkiewicz, P., Marée, A.F.M., Grieneisen, V.A., and Coen, E. (2013). An intracellular partitioning-based framework for tissue cell polarity in plants and animals. Development *140*, 2061–2074.

46. Nissen, S.B., Rønhild, S., Trusina, A., and Sneppen, K. (2018). Theoretical tool bridging cell polarities with development of robust morphologies. eLife *7*, e38407.

47. Kuchen, E.E., Fox, S., Barbier de Reuille, P., Kennaway, R., Bensmihen, S., Avondo, J., Calder, G.M., Southam, P., Robinson, S., Bangham, A., et al. (2012). Generation of Leaf Shape Through Early Patterns of Growth and Tissue Polarity. Science *335*, 1092–1096.

48. Xu, T., Wen, M., Nagawa, S., Fu, Y., Chen, J.-G., Wu, M.-J., Perrot-Rechenmann, C., Friml, J., Jones, A.M., and Yang, Z. (2010). Cell Surface- and Rho GTPase-Based Auxin

Signaling Controls Cellular Interdigitation in Arabidopsis. Cell *143*, 99–110.

49. Yang, Q., Wan, X., Wang, J., Zhang, Y., Zhang, J., Wang, T., Yang, C., and Ye, Z. (2020). The loss of function of HEL, which encodes a cellulose synthase interactive protein, causes helical and vine-like growth of tomato. Hortic. Res. *7*, 180.

50. Bünder, A., Sundman, O., Mahboubi, A., Persson, S., Mansfield, S.D., Rüggeberg, M., and Niittylä, T. (2020). CELLULOSE SYNTHASE INTERACTING 1 is required for wood mechanics and leaf morphology in aspen. Plant J. *103*, 1858–1868.

51. Landrein, B., Lathe, R., Bringmann, M., Vouillot, C., Ivakov, A., Boudaoud, A., Persson, S., and Hamant, O. (2013). Impaired Cellulose Synthase Guidance Leads to Stem Torsion and Twists Phyllotactic Patterns in Arabidopsis. Curr. Biol. *23*, 895–900.

52. Carvajal-Gonzalez, J.M., Balmer, S., Mendoza, M., Dussert, A., Collu, G., Roman, A.-C., Weber, U., Ciruna, B., and Mlodzik, M. (2015). The clathrin adaptor AP-1 complex and Arf1 regulate planar cell polarity in vivo. Nat. Commun. *6*, 6751.

53. Nemhauser, J.L., Feldman, L.J., and Zambryski, P.C. (2000). Auxin and ETTIN in Arabidopsis gynoecium morphogenesis. Development *127*, 3877–3888.

54. Mansfield, C., Newman, J.L., Olsson, T.S.G., Hartley, M., Chan, J., and Coen, E. (2018). Ectopic BASL Reveals Tissue Cell Polarity throughout Leaf Development in Arabidopsis thaliana. Curr. Biol. CB *28*, 2638-2646.e4.

55. Heisler, M.G., Hamant, O., Krupinski, P., Uyttewaal, M., Ohno, C., Jönsson, H., Traas, J., and Meyerowitz, E.M. (2010). Alignment between PIN1 Polarity and Microtubule Orientation in the Shoot Apical Meristem Reveals a Tight Coupling between Morphogenesis and Auxin Transport. PLoS Biol. *8*, e1000516.

56. Yamaguchi, N., Wu, M.-F., Winter, C.M., and Wagner, D. (2014). LEAFY and Polar Auxin Transport Coordinately Regulate Arabidopsis Flower Development. Plants *3*, 251–265.

57. Dye, N.A., Popović, M., Iyer, K.V., Fuhrmann, J.F., Piscitello-Gómez, R., Eaton, S., and Jülicher, F. (2021). Self-organized patterning of cell morphology via mechanosensitive feedback. eLife *10*, e57964.

58. Martin, E., Theis, S., Gay, G., Monier, B., Rouvière, C., and Suzanne, M. (2021). Arp2/3-dependent mechanical control of morphogenetic robustness in an inherently challenging environment. Dev. Cell *56*, 687-701.e7.

59. Hamant, O., Heisler, M.G., Jönsson, H., Krupinski, P., Uyttewaal, M., Bokov, P., Corson, F., Sahlin, P., Boudaoud, A., Meyerowitz, E.M., et al. (2008). Developmental Patterning by Mechanical Signals in Arabidopsis. Science *322*, 1650–1655.

60. Burian, A., Ludynia, M., Uyttewaal, M., Traas, J., Boudaoud, A., Hamant, O., and

Kwiatkowska, D. (2013). A correlative microscopy approach relates microtubule behaviour, local organ geometry, and cell growth at the Arabidopsis shoot apical meristem. J. Exp. Bot. *64*, 5753–5767.

61. Hervieux, N., Dumond, M., Sapala, A., Routier-Kierzkowska, A.-L., Kierzkowski, D., Roeder, A.H.K., Smith, R.S., Boudaoud, A., and Hamant, O. (2016). A Mechanical Feedback Restricts Sepal Growth and Shape in Arabidopsis. Curr. Biol. *26*, 1019–1028.

62. Baskin, T.I., Beemster, G.T.S., Judy-March, J.E., and Marga, F. (2004). Disorganization of Cortical Microtubules Stimulates Tangential Expansion and Reduces the Uniformity of Cellulose Microfibril Alignment among Cells in the Root of Arabidopsis. Plant Physiol. *135*, 2279–2290.

63. Boehm, B., Westerberg, H., Lesnicar-Pucko, G., Raja, S., Rautschka, M., Cotterell, J., Swoger, J., and Sharpe, J. (2010). The Role of Spatially Controlled Cell Proliferation in Limb Bud Morphogenesis. PLoS Biol. *8*, e1000420.

64. Alonso, J.M., Stepanova, A.N., Leisse, T.J., Kim, C.J., Chen, H., Shinn, P., Stevenson, D.K., Zimmerman, J., Barajas, P., Cheuk, R., et al. (2003). Genome-wide insertional mutagenesis of Arabidopsis thaliana. Science *301*, 653–657.

65. Hamant, O., Das, P., and Burian, A. (2019). Time-Lapse Imaging of Developing Shoot Meristems Using A Confocal Laser Scanning Microscope. In Plant Cell Morphogenesis: Methods and Protocols Methods in Molecular Biology., F. Cvrčková and V. Žárský, eds. (Springer), pp. 257–268.

66. Hartasánchez, D.A., Kiss, A., Battu, V., Dumond, M., Soraru, C., Delgado-Vaquera, A., Massinon, F., Brasó-Vives, M., Mollier, C., Dubrulle, N., et al. (2022). Robustness of organ morphology is associated with modules of co-expressed genes related to plant cell wall (Plant Biology).

67. Barbier de Reuille, P., Routier-Kierzkowska, A.-L., Kierzkowski, D., Bassel, G.W., Schüpbach, T., Tauriello, G., Bajpai, N., Strauss, S., Weber, A., Kiss, A., et al. (2015). MorphoGraphX: A platform for quantifying morphogenesis in 4D. eLife *4*, e05864.

68. Wuyts, N., Palauqui, J.-C., Conejero, G., Verdeil, J.-L., Granier, C., and Massonnet, C. (2010). High-contrast three-dimensional imaging of the Arabidopsis leaf enables the analysis of cell dimensions in the epidermis and mesophyll. Plant Methods *6*, 17.

69. Robitaille, T.P., Tollerud, E.J., Greenfield, P., Droettboom, M., Bray, E., Aldcroft, T., Davis, M., Ginsburg, A., Price-Whelan, A.M., Kerzendorf, W.E., et al. (2013). Astropy: A community Python package for astronomy. Astron. Astrophys. *558*, A33.

70. The Astropy Collaboration, Price-Whelan, A.M., Sipőcz, B.M., Günther, H.M., Lim,

P.L., Crawford, S.M., Conseil, S., Shupe, D.L., Craig, M.W., Dencheva, N., et al. (2018). The Astropy Project: Building an inclusive, open-science project and status of the v2.0 core package. Astron. J. *156*, 123.

71. Ruel, K., Nishiyama, Y., and Joseleau, J.-P. (2012). Crystalline and amorphous cellulose in the secondary walls of Arabidopsis. Plant Sci. *193–194*, 48–61.

72. Virtanen, P., Gommers, R., Oliphant, T.E., Haberland, M., Reddy, T., Cournapeau, D., Burovski, E., Peterson, P., Weckesser, W., Bright, J., et al. (2020). SciPy 1.0: fundamental algorithms for scientific computing in Python. Nat. Methods *17*, 261–272.

73. Smyth, D.R., Bowman, J.L., and Meyerowitz, E.M. (1990). Early flower development in Arabidopsis. Plant Cell *2*, 755–767.